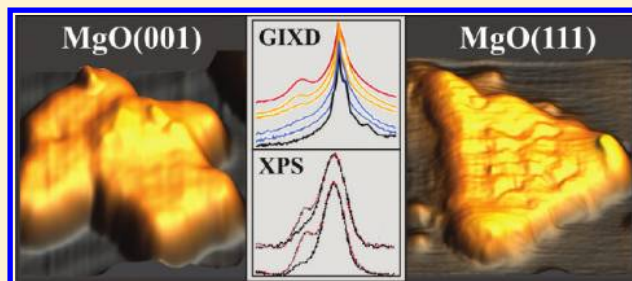


Competition between Polar and Nonpolar Growth of MgO Thin Films on Au(111)

S. Benedetti,^{†,‡,*} N. Nilius,^{§,*} P. Torelli,[‡] G. Renaud,^{||} H.-J. Freund,[§] and S. Valeri^{†,‡}[†]Dip. Fisica, Università di Modena e Reggio Emilia, Via Campi 213A, I-41125 Modena, Italy[‡]Centro S3, Istituto Nanoscienze—CNR, Via Campi 213A, I-41125 Modena, Italy[§]Fritz-Haber-Institut der Max-Planck-Gesellschaft, Faradayweg 4-6, D-14195 Berlin, Germany^{||}CEA-Grenoble, Institut Nanoscience et Cryogénie/SP2M/NRS, 17 rue de Martyrs, 38054 Grenoble, France

ABSTRACT: We report a growth study of MgO thin films on an Au(111) support, performed with scanning tunneling microscopy, X-ray photoelectron spectroscopy, and low-energy-electron and X-ray-diffraction techniques. Depending on the deposition temperature, the O₂ partial pressure, and the availability of water during oxide formation, two growth regimes can be distinguished. At high oxygen pressure, the MgO mainly adopts a square-lattice configuration and exposes the nonpolar (001) surface, whereas at low O₂ pressure a hexagonal lattice develops that resembles the (111) surface of rocksalt MgO. For

films beyond the monolayer limit, the emerging electrostatic dipole along the MgO(111) direction becomes important for the film morphology. Depending on the preparation conditions, the system takes either structural or adsorption-mediated routes to remove the polarity. Whereas surface roughening is identified as main polarity-compensation mechanism at perfect vacuum conditions, hydroxylation becomes important if water is present during oxide growth.



1. INTRODUCTION

Ideal polar oxide surfaces exhibit a nonvanishing dipole moment perpendicular to the surface, which arises from the alternation of oppositely charged lattice planes, as described by Tasker.¹ To compensate for this dipole moment, the surface responds in various ways, e.g., via reconstruction,^{2–4} rearrangement of the surface charges, or adsorption of charged ad-species (hydroxylation).^{5–7} In all scenarios, the surface charge-density changes in a way that the polarity-induced dipole gets canceled.⁸ The associated modifications in the surface properties render polar oxides attractive for various applications, ranging from catalysis, magnetism to the development of sensors and devices. In particular, the adsorption behavior and hence the chemical performance is largely affected by polar oxide terminations, as reflected in the unusual interaction of Au atoms with polar FeO/Pt(111) and in the enhanced decomposition rate of methanol on MgO(111) nanosheets.^{9,10} Detailed studies on polar oxides are still scarce, mainly because of difficulties in preparing model systems with well-defined dipole moments.^{11,12}

Whereas for bulk oxides, cancellation of the surface dipole is essential to stabilize the entire system, thin films can sustain finite dipole moments even without compensation.^{8,13} However, thin films also seek to lower their electrostatic energy, e.g., by reducing the separation of the oppositely charged layers.^{14–17} For MgO films with polar (111) orientation, theoretical and experimental studies suggested a structural transformation from the common rocksalt into the boron-nitride (B₁₂ or B_K) structure.^{14,18} In this configuration, the O and Mg planes do not

alternate along the surface normal anymore, but merge into single charge and dipole-compensated layers on the expense of an enlarged in-plane lattice parameter. Alternatively, the polar instability might be avoided by changes in the oxide stoichiometry,^{19,20} by metallization²¹ or hydroxylation of the oxide surface.²² In a heavily debated study, metallization was claimed to occur in an ultrathin MgO film despite the insulating character of the bulk material.^{14,23} Also, the metal substrate itself helps stabilizing polar configurations of an oxide ad-layer, either by inducing a depolarizing charge distribution at the interface or by fixing the oxide ions at the respective positions with the help of strong metal-oxide interactions.²⁴ Finally, adsorption-mediated routes are important for polarity compensation in thin oxide films.^{25,26} This is especially true for materials with a high affinity to water, such as MgO, where even the nonpolar termination readily develops an OH ad-layer.^{7,27}

In this work, we present a detailed study of the MgO growth behavior on the Au(111) surface. The substrate was chosen because of its small lattice mismatch with the polar oxide phase (+3.4%). We have investigated the basic mechanisms of the system to cancel polarity as well as their relevance at different thermodynamic conditions. Surprisingly, the formation of nonpolar MgO(001) patches turned out to be the most effective way despite the symmetry mismatch with the Au(111) surface.

Received: August 22, 2011**Revised:** October 8, 2011**Published:** October 09, 2011

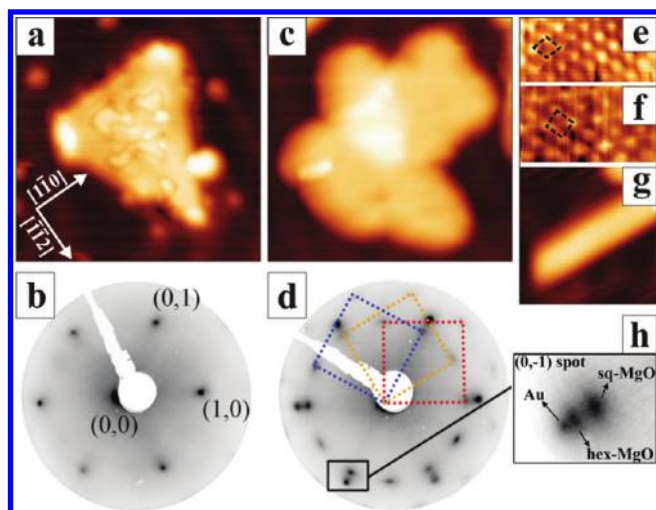


Figure 1. STM images (500 mV, $15 \times 15 \text{ nm}^2$) and respective LEED patterns (90 eV kinetic energy) of 0.5 ML MgO on Au(111) deposited at 500 K in (a,b) 5×10^{-7} mbar O_2 (O:Mg ratio = 60) and (c,d) 5×10^{-6} mbar O_2 (O:Mg ratio = 600). (e,f) Atomsically resolved STM images of the hexagonal (50 mV, $4.5 \times 2.1 \text{ nm}^2$) and square MgO phase (50 mV, $4.0 \times 2.2 \text{ nm}^2$). (g) STM image of an Au ad-island that has formed upon lifting the Au herringbone reconstruction during oxide growth (500 mV, $8 \times 8 \text{ nm}^2$). (h) Close-up of the (0,-1) LEED reflex with the different spots being assigned.

However, MgO(111) could also be stabilized at certain conditions and we will discuss how the polar instability is circumvented in this case.

2. EXPERIMENTAL SECTION

The experiments have been performed in two ultrahigh vacuum (UHV) chambers, having base pressures of about 2×10^{-10} mbar. The Au(111) substrate was prepared by cycles of sputtering and annealing at 750 K. The MgO films were produced by reactive deposition of Mg from a Mo crucible (evaporation rate $\approx 2 \text{ \AA}/\text{min}$), with the oxygen being introduced either via a nozzle in 10 mm distance to the sample or a leak valve. The cleanliness of the gas line was assured by carefully pumping the dosing system immediately before use. Sample annealing has been performed via electron bombardment; the temperature was monitored with a thermocouple placed in proximity to the crystal. The film stoichiometry was checked with XPS, using a nonmonochromatized Al-K α X-ray source and a hemispherical analyzer operated at $\pm 10^\circ$ angular and 1 eV energy resolution. STM measurements were performed with a custom-made beetle-type microscope operated at liquid-nitrogen temperature (100 K). Low-Energy-Electron-Diffraction (LEED) data were obtained with a three-grid system connected with a charge-coupled device camera. The structure of the MgO/Au(111) system was further investigated by means of Grazing Incidence X-ray Diffraction (GIXD). The measurements were performed in situ at the BM32 beamline at the ESRF, Grenoble, using a photon energy of 18 keV and a fixed incidence angle of $\alpha_i = 0.2^\circ$. All GIXD scans shown in this work are reported in Au reciprocal-lattice units (rlu), where h and k identify the (111) in-plane lattice and L is the axis perpendicular to the surface. The in-plane lattice parameters of the unreconstructed Au(111) and the bulk MgO(111) surface are 2.883 and 2.98 \AA , respectively.

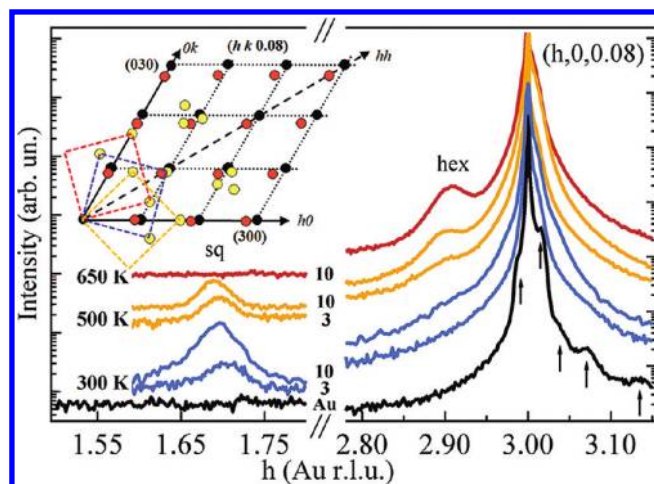


Figure 2. Radial GIXD scans along the $(h,0,0.08)$ direction for MgO films of various thickness (indicated on each curve, in ML). The growth has been performed in 1×10^{-7} mbar O_2 (O:Mg ratio = 30) and at 300 K (blue, bottom), 500 K (orange, middle), and 650 K (top, red). The bottom curve has been obtained on bare Au(111) and shows the fingerprints of the herringbone reconstruction as marked with arrows. All curves are shifted vertically for clarity. The inset displays a sketch of the reciprocal space of the system. Whereas the black dots represent the Au Bragg peaks, the red and yellow ones denote the *hex*- and *sq*-MgO phase, respectively.

3. RESULTS AND DISCUSSION

Depending on the preparation conditions, the growth of MgO on the Au(111) surface occurs in two different regimes. We will introduce the structural properties of both phases at the beginning of this chapter in section A, while the thermodynamic conditions for their stability are the focus of the second part B. In the following section C, the observed growth behavior is connected to the electrostatic dipole that emerges in the hexagonal but not the square phase of MgO. Possible dipole compensation schemes that become active in thicker films are finally discussed in section D.

(A). Introduction of the MgO Phases. Two growth regimes that mainly differ in the symmetry of the oxide lattice can be distinguished on the Au(111) surface. In the first mode, the sample morphology is governed by triangular and hexagonal MgO islands with a rather uniform size of $\sim 100 \text{ \AA}$ (Figure 1a). The mean island height amounts to 2.5 \AA , which roughly matches a single oxide layer (ML). Note that in the (111) direction, one ML always implies the presence of an Mg and an O plane. Many islands exhibit distinct protrusions on their top facet and at the corners, suggesting the development of a second oxide layer. The observed island shapes in the STM is compatible with a hexagonal symmetry of the oxide lattice. This is confirmed with atomsically resolved STM images and LEED measurements that display a simple 6-fold symmetric pattern (Figure 1b,e). The LEED reflexes arise from a superposition of the Au(111) and MgO spots, indicating a nearly epitaxial relationship of both lattices. Because of the hexagonal symmetry, we refer to this first growth mode as the hexagonal phase (*hex*-MgO).

The second regime differs from the first one in various aspects. The MgO forms islands with more than 100 \AA diameter and clearly three-dimensional (3D) shape (Figure 1c). The island edges often enclose angles of 45° and 90° , compared to 60° and 120° in the hexagonal phase. The LEED pattern is characterized

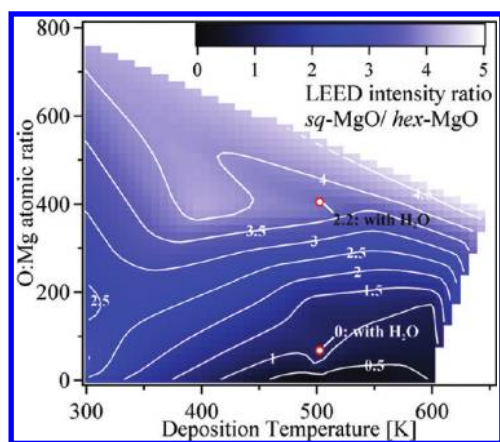


Figure 3. Ratio of the *sq*/*hex* LEED-spot intensities plotted as a function of temperature and O:Mg atomic ratio during oxide growth. The two red spots report the intensity ratio when 2×10^{-8} mbar of water is added to the reaction gas. The diagram has been produced from 27 MgO preparations on the Au(111) surface.

by additional spots in between the primitive Au(111) reflexes (Figure 1d), being explained by the presence of (001)-type oxide patches in three rotational domains. The square lattice-symmetry is in line with atomically resolved STM images and with the right angles that are frequently observed along the island perimeter (Figure 1c,f). We thus denote this second growth regime as the square phase (*sq*-MgO).

In most cases, neither the hexagonal nor the square configuration occur as a single phase, but both types coexist on the Au(111) surface. This becomes evident from the appearance of LEED spots that are specific to *hex*- and *sq*-MgO within one pattern. Focusing onto the (0, -1) reflex in Figure 1h, we observe three well-separated maxima. Whereas, the outermost spot is assigned to an Au(111) reflex, the central and inner ones belong to *hex*- and *sq*-MgO, respectively. In this assignment, the monolayer hexagonal phase has a +4% larger lattice parameter than Au(111), while the lattice constant of *sq*-MgO almost matches the one of gold (2.9 Å). The coexistence of *hex*- and *sq*-MgO is also suggested from GIXD measurements, which enable unambiguous distinction of the Au and MgO lattices due to a superior reciprocal-space resolution. Radial scans performed for MgO films of increasing thickness are reported in Figure 2 for the (*h*, 0, 0.08) direction in Au(111) reciprocal space. Besides the main Au Bragg peaks at 3 rlu, a distinct fine-structure is detected at higher rlu, which is assigned to the Au(111) herringbone reconstruction (see arrows in Figure 2). The extra features disappear at ~ 1.5 ML oxide thickness, indicating a lifting of the gold reconstruction during oxide growth. The released Au atoms nucleate in the form of elongated ad-islands at the gold step edges, as shown in Figure 1g. Additional Bragg peaks at ~ 2.91 rlu become visible only at higher MgO exposure. They are assigned to the hexagonal MgO phase and correspond to an in-plane lattice parameter of 3.0 Å. Their position in reciprocal space is marked by red dots in the inset of Figure 2. Other peaks are detected, e.g. at $h = 1.7$ and are compatible with the MgO(001) configuration. Their positions in reciprocal-space, as marked by yellow dots in Figure 2, translate into an in-plane lattice parameter of 2.88 Å, in good agreement with the LEED data for *sq*-MgO.

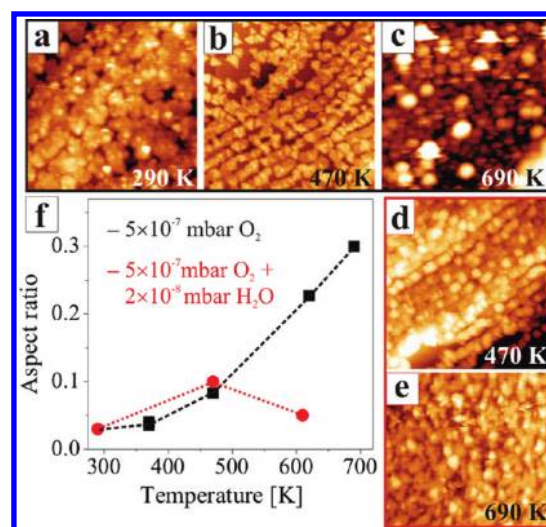


Figure 4. Evolution of the surface morphology with temperature for samples grown at (a–c) 5×10^{-7} mbar O_2 (O:Mg ratio = 60) and (d,e) in addition of 2×10^{-8} mbar water (2.5 V, 100×100 nm²). (f) Dependence of the aspect ratio of MgO islands on the temperature for the two preparation conditions (black: pure O_2 ; red: O_2 plus H_2O).

(B). Stability Range of Square and Hexagonal MgO. After having introduced the two main MgO configurations on the Au(111) surface, we will analyze the preparation conditions that lead to their occurrence. The explored growth parameters are the temperature, the O_2 partial pressure, and the availability of water during oxide formation. The effect of the latter has been studied in detail, because electrostatic dipoles that are known to emerge on the (111) terminated MgO surface are effectively removed via hydroxylation.⁸ To determine the stability of *sq*- versus *hex*-MgO at different preparation conditions, we have analyzed dozens of MgO films by means of three independent experimental techniques:

(i). **LEED.** The relative abundance of the two structural phases was derived from the intensity ratio of *sq*- and *hex*-MgO spots in the LEED patterns. We are aware that this procedure relies on a number of approximations, because the Au(111) reflexes cannot always be separated from the oxide spots and the degree of long-range order might be different in different preparations. We have tried to minimize these uncertainties by using samples with identical MgO coverage. Spot intensities have been determined by fitting a background-subtracted Gaussian to the experimental peaks and averaging over equivalent spots in the pattern. Figure 3 displays the resulting phase diagram, in which the *sq*/*hex* intensity ratio is plotted as a function of deposition temperature and O-to-Mg flux ratio during preparation. The Mg-atom flux is measured with a quartz microbalance and cross checked with quantitative XPS, whereas the estimation of the O-atom flux depends on the gas source. If dosing is performed with a nozzle placed in front of the sample, then all molecules will reach the surface and their number is directly determined from the total oxygen supply and the pumping speed of the system. If the gas is introduced by backfilling the chamber via a leak valve, then the O-flux is determined from the partial pressure read by the ion gauge (1 ML per second in 10^{-6} mbar O_2). We use the Mg-to-O flux ratio instead of the O_2 partial pressure in our analysis, as this parameter accounts for the local oxygen pressure directly at the sample surface.

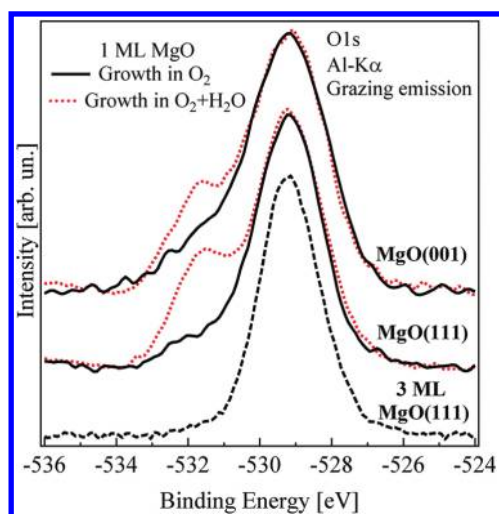


Figure 5. XPS O1s peak for *sq*-MgO (O:Mg = 400) and *hex*-MgO (O:Mg = 16) grown at 500 K. Continuous black lines indicate the peak shapes obtained for a growth in pure O₂, the red dotted spectra have been obtained by adding 2×10^{-8} mbar H₂O to the reaction gas. For comparison, the O1s peak for 3 ML *hex*-MgO is shown at the bottom ($T = 500$ K, O:Mg = 16).

(ii). *STM*. The abundance of the two phases has also been analyzed with STM, being a local probe. However, clear distinction between *sq* and *hex*-MgO was only possible in atomically resolved images, which were hard to obtain on a regular basis. A structural assignment based on the island morphologies was ambiguous due to the complex and irregular shapes of many oxide patches. We have therefore restricted our analysis to the evaluation of aspect (height to diameter) ratios of the MgO islands and the surface fraction covered by oxide at different preparation conditions (Figure 4).

(iii). *XPS*. The impact of hydroxylation on the stability of *sq*- and *hex*-MgO was determined by analyzing the shape of the O 1s peak in XPS. Two characteristic spectra obtained in the square ($T = 500$ K, O:Mg = 400) and hexagonal (O:Mg = 16) growth regime are plotted in Figure 5. Both curves exhibit a main peak at 529 eV, typical for O in MgO, and a shoulder at 531.5 eV that reflects the presence of OH. In absence of extra water, the OH coverage was determined with $\sim 7\%$ for both *sq* and *hex*-MgO monolayers (solid curves). It increases to around 25% when adding 2×10^{-8} mbar H₂O to the reaction gas (dotted curves).

Using these data sets, the stability regime for *sq*- and *hex*-MgO on the Au surface is determined. Apparently, the square configuration preferentially develops at high O₂ partial pressures, while the hexagonal phase is more stable at oxygen poor conditions (Figure 3). Independent of the lattice symmetry, the MgO patches show a strong tendency for vertical growth at higher temperature, while more or less homogeneous films develop upon room-temperature deposition (Figure 4a–c). The films become even flatter when water is added to the reaction gas (Figure 4d,e), while a perfect vacuum environment promotes the formation of 3D patches. The amount of OH groups is found to be similar on *sq*- and *hex*-MgO, suggesting the same incentive for hydroxylation in the monolayer regime. Evidently, hydroxylation is not crucial to stabilize the hexagonal oxide phase in the limit of an ultrathin film. In fact, the OH-concentration mainly depends on the growth temperature with the largest numbers found at 300 K.

(C). **Discussion.** Our experimental analysis provides a consistent picture for the stability range of *sq*- and *hex*-MgO on the Au(111) surface. According to Figure 3, the hexagonal phase prevails at low O:Mg ratios and temperatures between 400 and 700 K, while the square configuration preferentially develops in oxygen excess. Apparently, the O₂ partial pressure is the most crucial growth parameter, which might be explained in the following way. At oxygen-poor conditions, the incoming Mg most likely adjusts its adsorption site on the Au(111) surface before oxidation takes place. The growth is therefore governed by strong Au–Mg interactions, which favor the development of a hexagonal Mg lattice. The oxygen then interacts with the already existing Mg-island structure without changing its symmetry, resulting in the growth of a hexagonal oxide phase. The fixed lateral dimension of the (111)-type oxide islands of ~ 100 Å (Figure 1a) originates from the lattice mismatch with the Au(111) surface, which has been estimated to 4% with LEED and GIXD. Good interfacial registry is only realized in the center of each island, while the Mg ions are gradually pushed out of their preferred binding position as the growth proceeds. The subsequent need to occupy unfavorable lattice sites leads to a self-termination in the growth of hexagonal MgO islands.

With increasing O₂ partial pressure, the Mg and oxygen species have a higher probability to interact on the surface before compact Mg islands are formed. The growth is now dictated by the MgO lattice cohesion that is larger in the square phase due to the higher atom-coordination number, and not by the template effect of Au(111), as before. Oxygen-rich conditions therefore promote the growth of compact *sq*-MgO islands, irrespective of the symmetry mismatch with the Au support. The fact that already subtle changes in the preparation conditions alter the MgO equilibrium structure from hexagonal to square suggests that both phases are characterized by similar formation energies on the Au(111) surface. This degeneracy holds, however, only in the monolayer limit, because the electrostatic dipole that develops in *hex*-MgO modifies the energy landscape with increasing film thickness. We will address this issue in section D.

The temperature, as the second growth parameter, turns out to be less important, as the oxide phase that corresponds to the preset O₂ partial pressure develops in a wide temperature range. This observation is surprising at first glance, because the STM images in Figure 4 suggest a pronounced temperature effect on the oxide morphology. One possible explanation is that only the symmetry of the initial oxide nucleus decides on the growth mode, while subsequently arriving atoms arrange in a similar fashion. The nucleation process itself might be hardly affected by the deposition temperature. At low O₂ pressure, i.e., in the hexagonal mode, the enhanced atom mobility at high temperature helps establishing well-shaped Mg islands that can be oxidized later. In the square regime, on the other hand, the Mg–O units have a higher probability for up-step diffusion at high T, promoting the formation of thick MgO islands delimited by low-energy (001) facets. In general, the MgO growth behavior is most likely controlled by kinetic effects in our study, while the thermo-dynamically favored oxide configuration might not be realized in the accessible temperature range.

Finally, we want to discuss the role of water in stabilizing *sq*- and *hex*-MgO at different preparation conditions (Figure 5). Both square and hexagonal oxide films contain similar OH concentrations of $\sim 7\%$. This finding seems puzzling, because bulk MgO(111) is known to interact vigorously with water in order to compensate the polar dipole connected with this termination. In

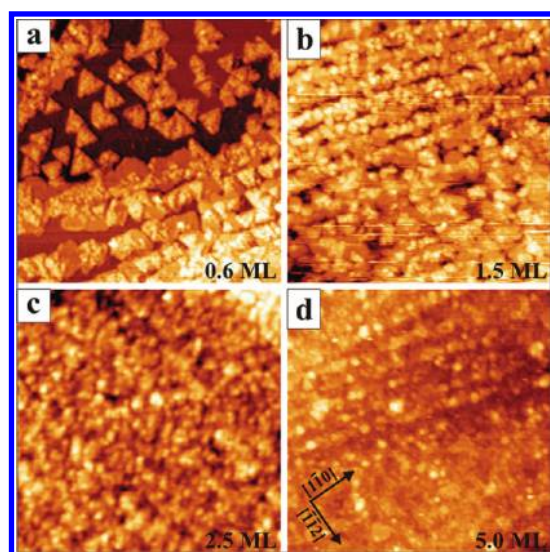


Figure 6. STM images (3.5 V , $100 \times 100\text{ nm}^2$) of four MgO films with increasing nominal thickness. The preparations have been performed at 500 K and $5 \times 10^{-7}\text{ mbar}$ O_2 partial pressure ($\text{O}:\text{Mg}$ ratio = 60).

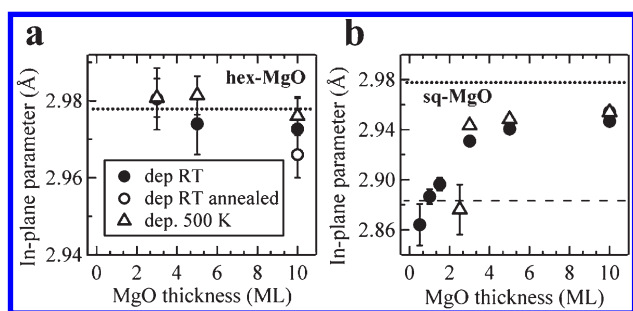


Figure 7. Evaluation of the in-plane lattice parameter for (a) *hex*-MgO and (b) *sq*-MgO films deposited at 300 K (dots), after annealing to 500 K (empty dots) and after deposition at 500 K (triangles). Dashed and dotted lines represent the bulk lattice constant for Au and MgO, respectively.

contrast, MgO(001) is less susceptible to hydroxylation due to a balanced charge-distribution at the surface.²⁷ The comparable hydroxylation potential of *sq*- and *hex*-MgO is however in line with recent theoretical studies on monolayer oxide films.^{24,28} Irrespective of the lattice symmetry, single-layer oxides on metal supports are only of induced-polar character, which means that any intrinsic dipole is largely suppressed due to a reduced separation of positively and negatively charged lattice planes.¹³ Conversely, a new dipole arises from the interfacial charge transfer, which occurs from the MgO film into the electronegative Au support in our case.²⁹ The associated accumulation of excess electrons in the metal triggers a polaronic distortion of the oxide lattice, in which the anions are pushed away from the interface while the cations move closer. The resulting dipole moment has the same magnitude as the one induced by the charge transfer, but an opposite sign. As the effect of induced-polarity is equally strong for *sq*- and *hex*-MgO, both monolayer films show the same affinity to bind water from the residual gas.²⁸ Deviations in the adsorption behavior might only arise from the lower coordination number of the O ions in *hex*- (3-fold) with respect to *sq*-MgO (4-fold) and from the presence of polar step

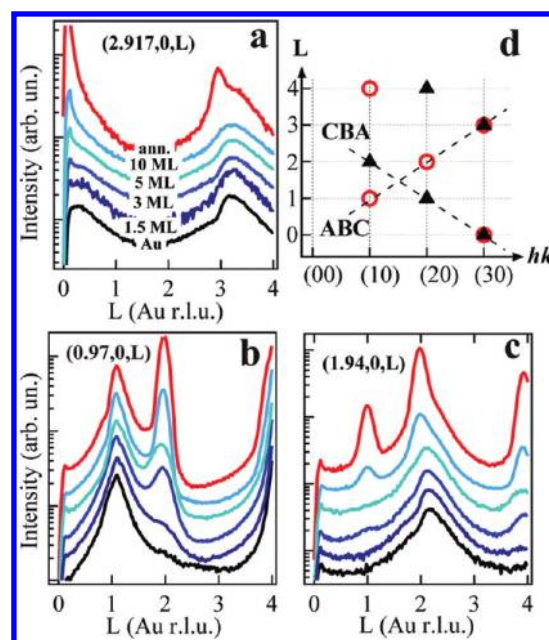


Figure 8. (a–c) GIXD scans along L for MgO films with increasing thickness. Three different rods are reported (in Au r.l.u.). (d) Sketch of the reciprocal space perpendicular to the surface indicating the position of the observed peaks (empty dots: ABC stacking; triangles: CBA stacking).

edges. However, those differences are most likely insufficient to alter the OH signal detected with XPS (Figure 5).

Only if the MgO growth is performed in a water background of $2 \times 10^{-8}\text{ mbar}$ (mixed with $5 \times 10^{-7}\text{ mbar}$ O_2), the surface OH concentration rises to 25% (Figure 5, dotted lines). Moreover, the extra water reduces the abundance of *sq*- compared to *hex*-MgO, as visualized by the extra points in the phase diagram of Figure 3. We attribute the enhanced stability of the hexagonal phase to the removal of polar borders that are intrinsic to the (111) lattice configuration. Also, the formation of other OH-rich configurations, such as $\text{Mg}(\text{OH})_2$ (brucite), cannot be excluded at those conditions.

(D). Thick MgO Films. In the last part of this work, we will address the morphological evolution of MgO/Au(111) films with increasing thickness. We mainly focus on the hexagonal phase, which is more interesting than square MgO because of the intrinsic dipole connected with this structure. For thick (001)-oriented films, we just note that they become increasingly rough, because the differently oriented MgO islands are unable to coalesce into a single-crystalline film. The thickness evolution of MgO(111) on the gold support is displayed in Figure 6. For 1–2 ML nominal thickness, triangular and hexagonal oxide islands are observed, as already discussed in A. Two island orientations, aligned with the Au[$\bar{1}\bar{1}2$] and $[11\bar{2}]$ direction, are discernible, which implies occupation of hcp and fcc hollow sites in the Au(111) surface by the incoming Mg atoms. With increasing exposure, a second and third MgO layer starts nucleating on the island top, although the mean island diameter increases only slightly. Above 2 ML exposure, individual islands merge into a closed but uneven film, which does not expose well-defined step edges. We will demonstrate below that this roughening is the main mechanism of *hex*-MgO to suppress the emerging electrostatic dipoles.

According to GIXD measurements, the MgO(111) lattice parameter decreases slightly with film thickness, reaching the bulk value at around 10 ML (Figure 7a). Changes in the deposition temperature or postannealing of the film hardly affect this behavior. Small square patches that are still present on the surface show the opposite trend, as their lattice parameter increases up to 5 ML nominal thickness. We believe that the reduced lattice constant of *sq*-MgO is governed by a fixed interface relation between the (001) monolayer and the Au(111) surface, which has been identified as a (6×1) superstructure in a recent STM study.²⁹ Also the layer stacking in *hex*-MgO can be deduced from GIXD scans performed perpendicular to the surface (L scans). Respective scans along the (30 L), (10 L), and (20 L) directions in MgO reciprocal-space are reported in Figure 8. The (30 L) scan reveals a periodicity of three in the sequence of MgO Bragg peaks, similar to the Au case (black curve), which indicates an out-of-plane symmetry typical for fcc or rocksalt lattices. In (10 L) and (20 L) scans, not only the main peaks at $L = 1$ and $L = 4$ (10 L) and $L = 2$ (20 L) are detected, but additional maxima occur at $L = 2$ and $L = 1$ and 4 along the (10 L) and (20 L) directions, respectively. Those extra peaks suggest the presence of MgO patches with a reversed fcc stacking as compared to the regular domains and the Au sequence. The presence of two stacking domains is in agreement with the STM images that also show triangular MgO islands with two orientations (Figure 6a). We finally note that all Bragg peaks appear close to integer values in the L scans, reflecting that the out-of-plane lattice parameter of MgO(111) is close to the Au(111) value of 2.35 Å. This result is compatible with a small compression of the interlayer distance in the film with respect to bulk MgO (2.4 Å). On the basis of these results and earlier discussions in the literature,⁸ we can address the polarity issue in thick MgO(111) films:

(i). *Structural Modifications.* DFT calculations found the boron-nitride structure with cations and anions being in the same plane to be the energetically favored configuration for both, free-standing and supported MgO films.¹⁸ The drastically reduced interlayer distance in this case would induce a substantial increase of the in-plane lattice parameter, a prediction that can be accurately checked in our experiment. Indeed, LEED and GIXD data revealed a larger lattice constant for *hex*-MgO; however, the measured increase of +3.4% remains well below the expected expansion of 13% in the boron-nitride case which renders this compensation mechanism unlikely. Two other observations support this conclusion. Although the out-of-plane parameter measured for 10 ML MgO(111) is a few percent smaller than the bulk value, this reduction is clearly incompatible with the coplanar situation. And, the boron-nitride structure should exhibit additional peaks with a periodicity of two in the L scans. Conversely, a zincblend lattice induces peaks at even and odd L values with alternating intensities and shapes. Both signatures are not observed in our GIXD data and we consequently exclude a massive restructuring of the MgO rocksalt lattice.

(ii). *Hydroxylation.* Also hydroxylation seems to be unimportant to cancel the polarity of *hex*-MgO films. This conclusion is drawn from the low OH concentrations detected for thick MgO(111) films prepared in the absence of water (see lower curve in Figure 5). The measured quantities are insufficient to produce the closed-packed OH layer that would be required for dipole removal.⁸ The small impact of surface hydroxylation is not surprising for an UHV experiment with limited availability of water and not in conflict with the general importance of

OH groups for stabilizing polar surfaces.^{5,8,22} The situation only changes if extra water is dosed upon oxide formation and the OH concentration rises to almost half a monolayer. In this coverage regime, surface hydroxylation becomes indeed relevant for suppressing the polar dipole, yet it needs to be complemented by alternative means. We note however that the additional water gives rise to a largely reduced roughness of *hex*-MgO films, as discussed next (see Figure 4).

(iii). *Surface Roughening.* Morphological changes in the MgO(111) surface therefore remain as the most likely mechanism to suppress uncompensated polarity. This depolarization scheme is based on the formation of small nonstoichiometric units that produce exactly the amount of extra charges that is required for dipole compensation. The best studied dipole-removing ad-structure is the octupolar reconstruction that has been predicted by theory³⁰ and was later experimentally confirmed on the MgO(111) and NiO(111) surface.^{2,7} The reconstruction comprises two-layer high pyramids that are arranged on a regular (2×2) grid and exhibit four positive (negative) excess charges for the magnesium (oxygen) rich composition. Although well-defined nanostructures are not revealed on the MgO(111) films, we believe that the surface roughening fulfills a similar function as each protrusion represents a nonstoichiometric unit that alters the charge density. Spatial ordering of those units is not achieved in our case, because the Au(111) substrate does not withstand the required annealing temperatures to order the ad-islands.

We finally note that also the development of O–Mg–O trilayers, being another theoretical concept for polarity cancellation,³¹ cannot be reconciled with our experimental results. Although XPS reveals a slight oxygen excess in our MgO films, the magnitude is incompatible with the formation of an extra O-layer bound to the surface.

4. CONCLUSIONS

Using different experimental techniques, we have analyzed the growth of MgO thin films on an Au(111) support. Depending on the preparation conditions, e.g., the O₂ partial pressure, deposition temperature, and water ambience, we observe the formation of oxide structures with either square or hexagonal lattice symmetry. Whereas at higher oxygen pressure, the MgO(001) phase is preferred due to the establishment of stable Mg–O bonds in the initial growth regime, a lower pressure promotes the formation of MgO(111) patches. The hexagonal phase is stabilized by the development of Au–Mg interfacial bonds that imprint the lattice symmetry of the substrate onto the growing oxide film. Compared to the oxygen pressure, the temperature and water presence were found to be of minor importance for the realized growth regime.

Whereas monolayer films of both (001) and (111) type are only of induced-polar character, a strong dipole develops upon thickening the (111) oxide patches. The divergence in the electrostatic potential is inhibited in our case by surface roughening, involving the formation of small nonstoichiometric units on top of the flat film. Spontaneous hydroxylation, as an alternative compensation scheme, is inefficient at the vacuum environment of our experiment. Only intentional water dosing during film growth produces considerable amounts of OH on the oxide surface and causes the film roughness to decrease. In general, the (111)-oriented MgO films prepared in our study need to be improved to obtain the structural quality that would be required

for adsorption and nucleation experiments performed on potentially polar oxide surfaces.

AUTHOR INFORMATION

Corresponding Author

*E-mail: stefania.benedetti@unimore.it (S.B.); nilius@fhi-berlin.mpg.de (N.N.).

ACKNOWLEDGMENT

The authors thank the Fondazione Cassa di Risparmio di Modena for financial support. We are grateful to Jacek Goniakowski for many insightful discussions.

REFERENCES

- (1) Tasker, P. W. *J. Phys. C: Solid State Phys.* **1979**, *12*, 4977–4984.
- (2) Barbier, A.; Mocuta, C.; Kuhlbeck, H.; Peters, K. F.; Richter, B.; Renaud, G. *Phys. Rev. Lett.* **2000**, *84*, 2897–2900.
- (3) Dulub, O.; Diebold, U.; Kresse, G. *Phys. Rev. Lett.* **2003**, *90*, 016102.
- (4) Ostendorf, F.; Torbrügge, S.; Reichling, M. *Phys. Rev. B* **2008**, *77*, 041405(R).
- (5) Wang, Y. Z. *Phys. Chem.* **2008**, *222*, 927–966.
- (6) Lazarov, V. K.; Plass, R.; Poon, H. C.; Saldin, D. K.; Weinert, M.; Chambers, S. A.; Gajdardziska-Josifovska, M. *Phys. Rev. B* **2005**, *71*, 115434.
- (7) Barbier, A.; Stierle, A.; Finocchi, F.; Jupille, J. *J. Phys.: Condens. Matter* **2008**, *20* (184014), 1–13.
- (8) Goniakowski, J.; Finocchi, F.; Noguera, C. *Rep. Prog. Phys.* **2008**, *71* (016501), 1–55.
- (9) Nilus, N.; Rienks, E. D. L.; Rust, H.-P.; Freund, H.-J. *Phys. Rev. Lett.* **2005**, *95*, 066101.
- (10) Hu, J.; Zhu, K.; Chen, L.; Kübel, C.; Richards, R. J. *Phys. Chem. C* **2007**, *111*, 12038–12044.
- (11) Mantilla, M.; Jedrecy, N.; Lazzari, R.; Jupille, J. *Surf. Sci.* **2008**, *602*, 3089–3094.
- (12) Nilus, N. *Surf. Sci. Rep.* **2009**, *64*, 595–659.
- (13) Goniakowski, J.; Noguera, C.; Giordano, L. *Phys. Rev. Lett.* **2007**, *98*, 205701.
- (14) Kiguchi, M.; Entani, S.; Saiki, K.; Goto, T.; Koma, A. *Phys. Rev. B* **2003**, *68*, 115402.
- (15) Tusche, C.; Meyerheim, H. L.; Kirschner, J. *Phys. Rev. Lett.* **2007**, *99*, 026102.
- (16) Kim, Y. J.; Westphal, C.; Ynzunza, R. X.; Galloway, H. C.; Salmeron, M.; van Hove, M. A.; Fadley, C. S. *Phys. Rev. B* **1997**, *55*, 13448–13451.
- (17) Meyer, W.; Hock, D.; Biedermann, K.; Gubo, M.; Müller, S.; Hammer, L.; Heinz, K. *Phys. Rev. Lett.* **2008**, *101*, 016103.
- (18) Goniakowski, J.; Noguera, C. *Phys. Rev. Lett.* **2004**, *93*, 215702.
- (19) Hebenstreit, W.; Schmidt, M.; Redinger, J.; Podloucky, R.; Varga, P. *Phys. Rev. Lett.* **2000**, *85*, 5376–5379.
- (20) Meyer, W.; Biedermann, K.; Gubo, M.; Hammer, L.; Heinz, K. *J. Phys.: Condens. Matter* **2008**, *20* (265011), 1–6.
- (21) Arita, R.; Tanida, Y.; Entani, S.; Kiguchi, M.; Saiki, K.; Aoki, H. *Phys. Rev. B* **2004**, *69*, 235423.
- (22) Rohr, F.; Wirth, K.; Libuda, J.; Cappus, D.; Bäumer, M.; Freund, H.-J. *Surf. Sci.* **1994**, *315*, L977–L982.
- (23) Xue, M.; Guo, Q. J. *Chem. Phys.* **2007**, *127*, 054705.
- (24) Goniakowski, J.; Giordano, L.; Noguera, C. *Phys. Rev. B* **2010**, *81*, 205404.
- (25) Kitakatsu, N.; Maurice, V.; Marcus, P. *Surf. Sci.* **1998**, *411*, 215–230.
- (26) Knudsen, J.; Merte, L. R.; Grabow, L. C.; Eichhorn, F. M.; Porsgaard, S.; Zeuthen, H.; Vang, R. T.; Lægsgaard, E.; Mavrikakis, M.; Besenbacher, F. *Surf. Sci.* **2010**, *604*, 11–20.
- (27) Altieri, S.; Contri, S. F.; Valeri, S. *Phys. Rev. B* **2007**, *76*, 205413.
- (28) Goniakowski, J.; Noguera, C. *Phys. Rev. B* **2009**, *79*, 15543.
- (29) Pan, Y.; Benedetti, S.; Nilus, N.; Freund, H.-J. *Phys. Rev. B* **2011**, *84*, 075456.
- (30) Wolf, D. *Phys. Rev. Lett.* **1992**, *68*, 3315–3319.
- (31) Giordano, L.; Lewandowski, M.; Groot, I. M. N.; Sun, Y. N.; Goniakowski, J.; Noguera, C.; Shaikhutdinov, S.; Pacchioni, G.; Freund, H. J. *J. Phys. Chem. C* **2010**, *114*, 21504–21509.